



Universiteit
Leiden
The Netherlands

SOFIA feedback survey: PDR diagnostics of stellar feedback in different regions of RCW 49

Tiwari, M.; Wolfire, M.; Pound, M.W.; Tarantino, E.; Karim, R.; Bonne, L.; ... ; Tielens, A.G.G.M.

Citation

Tiwari, M., Wolfire, M., Pound, M. W., Tarantino, E., Karim, R., Bonne, L., ... Tielens, A. G. G. M. (2022). SOFIA feedback survey: PDR diagnostics of stellar feedback in different regions of RCW 49. *The Astronomical Journal*, 164(4). doi:10.3847/1538-3881/ac8a44

Version: Publisher's Version

License: [Creative Commons CC BY 4.0 license](https://creativecommons.org/licenses/by/4.0/)

Downloaded from: <https://hdl.handle.net/1887/3514825>

Note: To cite this publication please use the final published version (if applicable).



SOFIA FEEDBACK Survey: PDR Diagnostics of Stellar Feedback in Different Regions of RCW 49

M. Tiwari^{1,2}, M. Wolfire¹, M. W. Pound¹, E. Tarantino¹, R. Karim¹, L. Bonne³, C. Buchbender⁴, R. Güsten², C. Guevara⁴, S. Kabanovic⁴, Ü. Kavak³, M. Mertens⁴, N. Schneider⁴, R. Simon⁴, J. Stutzki⁴, and A. G. G. M. Tielens^{1,5}

¹ University of Maryland, Department of Astronomy, College Park, MD 20742-2421, USA; mtiwari@umd.edu

² Max-Planck Institute for Radioastronomy, Auf dem Hügel, D-53121 Bonn, Germany

³ SOFIA Science Center, USRA, NASA Ames Research Center, M.S. N232-12, Moffett Field, CA 94035, USA

⁴ I. Physik. Institut, University of Cologne, Zùlpicher Str. 77, D-50937 Cologne, Germany

⁵ Leiden Observatory, Leiden University, PO Box 9513, 2300 RA Leiden, The Netherlands

Received 2022 March 25; revised 2022 August 15; accepted 2022 August 15; published 2022 September 21

Abstract

We quantified the effects of stellar feedback in RCW 49 by determining the physical conditions in different regions using the [C II] 158 μm and [O I] 63 μm observations from SOFIA, the ^{12}CO (3–2) observations from APEX, and the H_2 line observations from Spitzer telescopes. Large maps of RCW 49 were observed with the SOFIA and APEX telescopes, while the Spitzer observations were only available toward three small areas. From our qualitative analysis, we found that the H_2 0–0 $S(2)$ emission line probes denser gas compared to the H_2 0–0 $S(1)$ line. In four regions (“northern cloud,” “pillar,” “ridge,” and “shell”), we compared our observations with the updated PDR Toolbox models and derived the integrated far-ultraviolet flux between 6 and 13.6 eV (G_0), H nucleus density (n), temperatures, and pressures. We found the ridge to have the highest G_0 (2.4×10^3 Habing units), while the northern cloud has the lowest G_0 (5×10^2 Habing units). This is a direct consequence of the location of these regions with respect to the Wd2 cluster. The ridge also has a high density ($6.4 \times 10^3 \text{ cm}^{-3}$), which is consistent with its ongoing star formation. Among the Spitzer positions, we found the one closest to the Wd2 cluster to be the densest, suggesting an early phase of star formation. Furthermore, the Spitzer position that overlaps with the shell was found to have the highest G_0 , and we expect this to be a result of its proximity to an O9V star.

Unified Astronomy Thesaurus concepts: Photodissociation regions (1223); Stellar feedback (1602); Molecular clouds (1072)

1. Introduction

Stellar feedback is one of the most important ingredients in the evolution of the interstellar medium (ISM). In particular, massive stars play a key role in regulating different feedback mechanisms (for recent observational studies see Pabst et al. 2019; Luisi et al. 2021; Tiwari et al. 2021; Kavak et al. 2022). They inject immense amounts of energy into their surroundings through stellar winds and through extreme-ultraviolet (EUV, $h\nu > 13.6 \text{ eV}$) and far-UV (FUV, $6 \text{ eV} < h\nu < 13.6 \text{ eV}$) photons. The EUV photons ionize gas ($\text{H} \rightarrow \text{H}^+$) in the vicinity of a star, giving rise to H II regions. The FUV photons heat the gas via the photoelectric effect on small grains and polycyclic aromatic hydrocarbon (PAHs), dissociate molecules, and ionize atoms, e.g., $\text{C} \rightarrow \text{C}^+$, giving rise to photodissociation regions (PDRs). This mechanical and radiative energy input catalyzes various physical and chemical processes, which shape the dense and diffuse gas into molecular clouds and into structures like shells and pillars. These structures vary in their physical conditions based on their location with respect to the illuminating source and on the geometry of the surrounding medium.

Determination of physical conditions in these molecular clouds, shells, and pillars is done through various chemical species. Neutral atomic gas in the ISM cools mainly at far-IR

(FIR) wavelengths through [C II] (158 μm) and [O I] (63 and 145 μm) line emission and probes regions predominantly at $A_v < 3$. Molecular gas cooling is dominated by ^{12}CO rotational emission, which probes regions at larger A_v (for details see Hollenbach & Tielens 1999; Wolfire et al. 2003, 2022).

RCW 49 is one of the most luminous massive-star-forming regions in our Galaxy. It is located at a distance of $4.16 \pm 0.33 \text{ kpc}$ (Vargas Álvarez et al. 2013; Zeidler et al. 2015; see also discussion in Tiwari et al. 2021), close to the tangent of the Carina arm at $l = 284^\circ.3$, $b = -0^\circ.3$. RCW 49 hosts a compact stellar cluster, Westerlund 2 (Wd2), consisting of 37 OB stars and 30 early-type OB star candidates surrounding it (Ascenso et al. 2007; Tsujimoto et al. 2007; Rauw et al. 2011; Mohr-Smith et al. 2015; Zeidler et al. 2015). There are two Wolf-Rayet stars also associated with RCW 49: WR20a, which is a part of the Wd2 cluster and is suggested to be among the most massive binaries in the Galaxy (Rauw et al. 2005), and WR20b, which is a few arcminutes away southeast of Wd2. Winds and radiation from these stars are responsible for sculpting the gas and dust into dense molecular clouds, shells, and pillars in RCW 49.

RCW 49 has been studied previously at radio, submillimeter, IR, and X-ray wavelengths. Whiteoak & Uchida (1997) and Benaglia et al. (2013) studied radio data (at 0.843, 1.38, 2.38, 5.5, 9 GHz) and reported two shells toward RCW 49. Furukawa et al. (2009) obtained ^{12}CO (2–1) data with the NANTEN2 telescope toward RCW 49. With an angular resolution of $1/5$, they identified two large-scale molecular clouds in velocity ranges of -11 to 9 km s^{-1} and 11 – 21 km s^{-1} and suggested



Original content from this work may be used under the terms of the [Creative Commons Attribution 4.0 licence](https://creativecommons.org/licenses/by/4.0/). Any further distribution of this work must maintain attribution to the author(s) and the title of the work, journal citation and DOI.

that their collision led to the formation of the Wd2 cluster. Ohama et al. (2010) analyzed ^{12}CO (1–0), ^{12}CO (2–1), and ^{13}CO (2–1) to estimate temperature and density distributions for the two clouds identified by Furukawa et al. (2009). Churchwell et al. (2004) studied RCW 49 at mid-IR wavelengths (Infrared Array Camera data at 3.6, 4.5, 5.8, and 8.0 μm) and identified different regions based on dust emission with respect to the angular radius from Wd2. Moreover, diffuse X-ray observations (0.5–7 keV) probed the hot plasma distributed around Wd2 (Townsend et al. 2019).

Although the studies mentioned above unveiled the rich region of RCW 49, the observations used for the analysis lacked either spatial or spectral resolution, which hindered precise investigation of the morphology, energetics, and physical conditions. The new high-resolution [C II] 158 μm and [O I] 63 μm observations toward RCW 49 were taken as part of the Stratospheric Observatory For Infrared Astronomy (SOFIA; Young et al. 2012) legacy program FEEDBACK⁶ (Schneider et al. 2020), and the ^{12}CO observations were taken with the Atacama Pathfinder Experiment (APEX;⁷ Güsten et al. 2006). In our previous work, we characterized the expanding shell of RCW 49 using the [C II], ^{12}CO , and ^{13}CO observations (Tiwari et al. 2021). With the goal of quantifying radiative and mechanical input by massive stars into their surroundings, similar studies were performed to understand the stellar feedback mechanisms in the ISM through the FEEDBACK program (first scientific results in Luisi et al. 2021; Tiwari et al. 2021; Beuther et al. 2022; Kabanovic et al. 2022).

In this paper, we quantify the effects of stellar feedback on different regions of RCW 49 by determining their physical conditions. We want to understand the contribution of stellar feedback in the evolution of these regions in terms of morphology and future star formation. We compare our observations (obtained through the FEEDBACK program and through the Spitzer telescope) with PDR models to derive the FUV incident flux (G_0), density (n), surface temperature (T_{surf}), and pressure (p) in different regions of RCW 49. Moreover, through this paper, we aim at providing a suitable PDR analysis strategy that can be used to determine the physical conditions in the ISM.

2. Observations

2.1. SOFIA

The [C II] and [O I] observations were observed during three flights in 2019 June using upGREAT⁸ (Risacher et al. 2018). The upGREAT receiver can observe both [C II] and [O I] lines simultaneously by using a dual 7-pixel low-frequency array (LFA) that was tuned to the [C II] line and, in parallel, a 7-pixel high-frequency array (HFA) that was tuned to the [O I] 63 μm line. The observing mode was driven by the [C II] line sensitivity, thus limiting the signal-to-noise ratio of the [O I] line. Moreover, the [O I] data were undersampled (for more details see Schneider et al. 2020).

A Fast Fourier Transform Spectrometer (FFTS) with 4 GHz instantaneous bandwidth and a frequency resolution of

0.244 MHz (Klein et al. 2012) served as the back end. Thus, both the [C II] and [O I] data have an original resolution of 0.04 km s^{-1} . The data set was then rebinned to a spectral resolution of 0.2 km s^{-1} . The instrument and telescope optics determine the intrinsic half-power beam widths: $14''.1$ for the [C II] line and $6''.3$ for the [O I] line. All spectra are presented on a main-beam brightness temperature (T_{mb}) scale. The main-beam efficiency (η_{mb}) values for [C II] and [O I] are 0.65 and 0.69, respectively. Further observational details are given in Tiwari et al. (2021).

2.2. APEX

The $J=3-2$ transition of ^{12}CO and ^{13}CO was observed toward RCW 49 using the LAsMA array on the APEX telescope (Güsten et al. 2006). The beamwidth is $18''.2$ at 345.8 GHz. Advanced FFTSs (Klein et al. 2012) are used as back ends with a bandwidth of $2 \times 4 \text{ GHz}$ and a native spectral resolution of 61 kHz. All spectra are calibrated in T_{mb} with $\eta_{\text{mb}} = 0.68$ at 345.8 GHz. After a linear baseline subtraction, all data were binned to 0.2 km s^{-1} . The angular resolution of the maps is $\sim 20''$. All other data sets were convolved to this resolution for the PDR analysis described later in this paper. For more observational details, see Tiwari et al. (2021).

2.3. Spitzer

The H_2 observations were carried out using the Infrared Spectrograph (IRS; Houck et al. 2004) on board the Spitzer Space Telescope (Werner et al. 2004). The H_2 0–0 $S(1)$ and H_2 0–0 $S(2)$ line data presented in this paper are part of the Spitzer program PID 20012 (PI M. Wolfire). The program observed seven fields (Castellanos et al. 2014), and we analyzed three (p1, p3, and p7) of them as shown in Figure 1. The AOR keys of each of them are 13812992, 13813504, and 13814528. The spectrograph observes in four modes depending on the wavelengths and resolution (Houck et al. 2004): short wavelengths with low resolution (SL), long wavelengths with low resolution (LL), short wavelengths with high resolution (SH), and long wavelengths with high resolution (LH). The $S(1)$ and $S(2)$ lines are at 17.03 and 12.28 μm observed with the SH mode. The pixel size is $2''.26$, the slit size is $4''.7 \times 11''.3$, and the mapped regions are $\sim 50'' \times 60''$ for p1, $\sim 50'' \times 50''$ for p3, and $\sim 40'' \times 40''$ for p7.

Observation data cubes (along with uncertainty cubes) were generated with the CUBE Builder for IRS Spectra Maps (CUBISM;⁹ Smith et al. 2007a), which is a tool used for constructing data cubes of the mapping mode spectra taken with the Spitzer IRS spectrograph. We then used PAHFIT¹⁰ (Smith et al. 2007b) on the data cubes, which decomposes the IRS spectra in order to give us intensity values at each pixel such that we have H_2 intensity and uncertainty maps.

3. Source Selection in RCW 49

Figure 1 shows RCW 49 marked with seven different regions (in white boxes), which are spatially and in some cases spectrally distinct. These regions are at different distances to the Wd2 cluster, and some have very distinct morphology, making them ideal to study the impact of stellar feedback in

⁶ <https://feedback.astro.umd.edu/>

⁷ APEX is a collaboration between the Max-Planck-Institut für Radioastronomie, Onsala Space Observatory, and European Southern Observatory.

⁸ German Receiver for Astronomy at Terahertz. (up)GREAT is a development by the MPI für Radioastronomie and the KOSMA/Universität zu Köln, in cooperation with the DLR Institut für Optische Sensorsysteme.

⁹ <https://irsa.ipac.caltech.edu/data/SPITZER/docs/dataanalysis/tools/cubism/>

¹⁰ <http://tir.astro.utoledo.edu/jdsmith/research/pahfit.php>

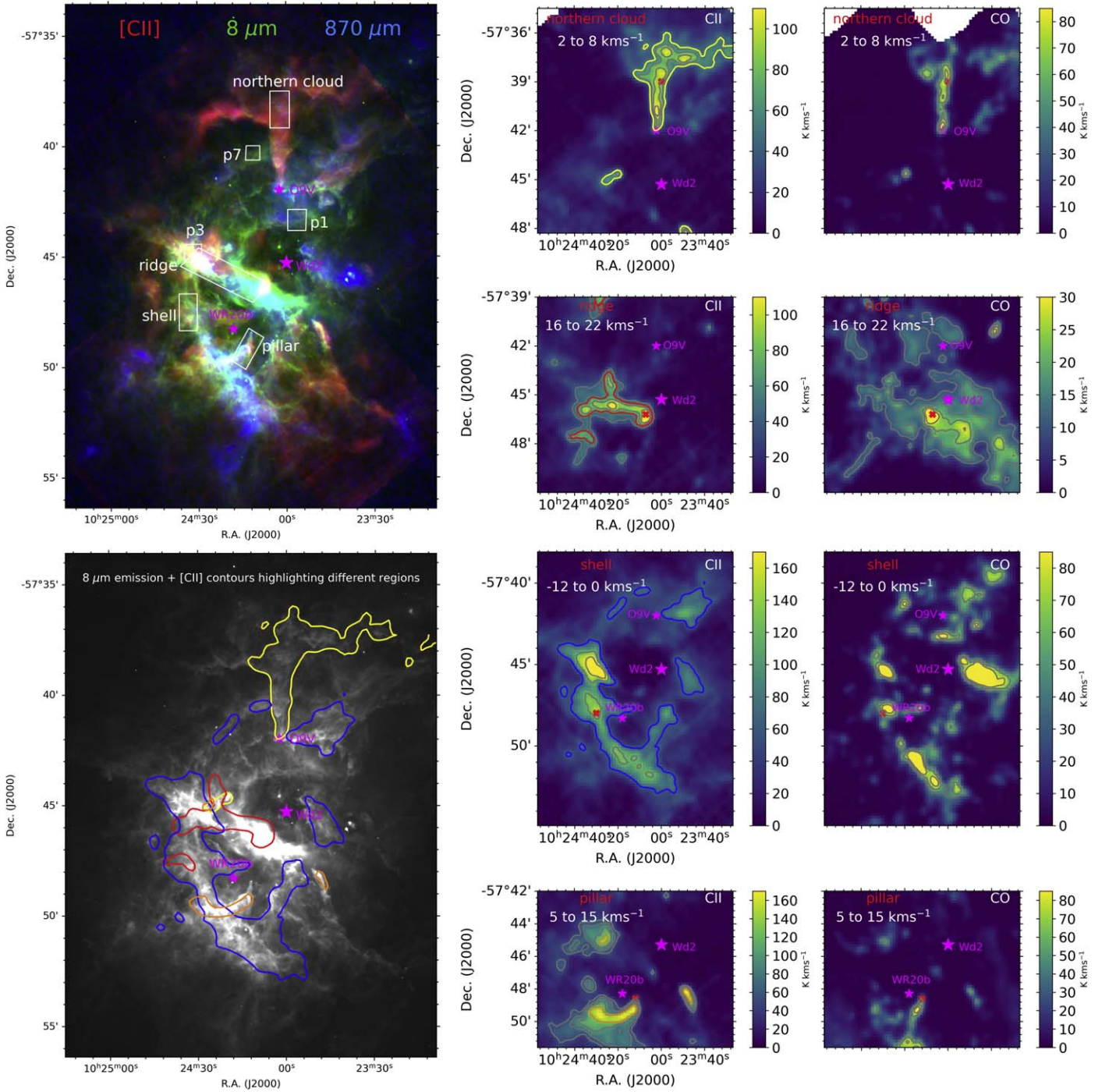


Figure 1. A red-blue-green (RBG) image of RCW 49 is shown in the top left panel. Red corresponds to the [C II] integrated intensity emission within the velocity range of -30 to 30 km s^{-1} . Green corresponds to the GLIMPSE (Benjamin et al. 2003) $8 \mu\text{m}$ emission, and blue corresponds to the ATLASGAL (Schuller et al. 2009) $870 \mu\text{m}$ continuum. Different interesting regions toward which the PDR analysis is done are shown and outlined with white boxes. The [C II] and ^{12}CO emissions toward the northern cloud, ridge, shell, and pillar are shown in the middle and right panels, respectively. The red crosses mark the lines of sight for which the spectra are presented in Figure 3. In the bottom left panel, the $8 \mu\text{m}$ emission image is overlaid with [C II] emission contours highlighting these regions. The contour colors are the same as the ones in the [C II] maps shown in the middle panels. The Wd2 cluster, the WR20b star, and the O9V star are shown in pink in all panels.

RCW 49. In this section we introduced these different regions by describing their physical and chemical characteristics.

We have selected the “northern cloud” as representative of the cloud whose collision with another cloud may have triggered the formation of the Wd2 cluster (Furukawa et al. 2009). This cloud can be spatially disentangled through its velocity range ($2\text{--}8 \text{ km s}^{-1}$). The “ridge” position was selected as part of the other cloud that is thought to have been involved

in the cloud collision that gave rise to the formation of Wd2 (Furukawa et al. 2009). Part of the ridge is associated with the inner dust ring identified in the Spitzer study of RCW 49 (Churchwell et al. 2004). The velocity of the ridge is in the range $16\text{--}22 \text{ km s}^{-1}$. We have selected a region in the “shell” that was identified by Tiwari et al. (2021) as expanding toward us at 12 km s^{-1} . This particular position is well separated from the ridge and pillar positions included in our analysis. The shell

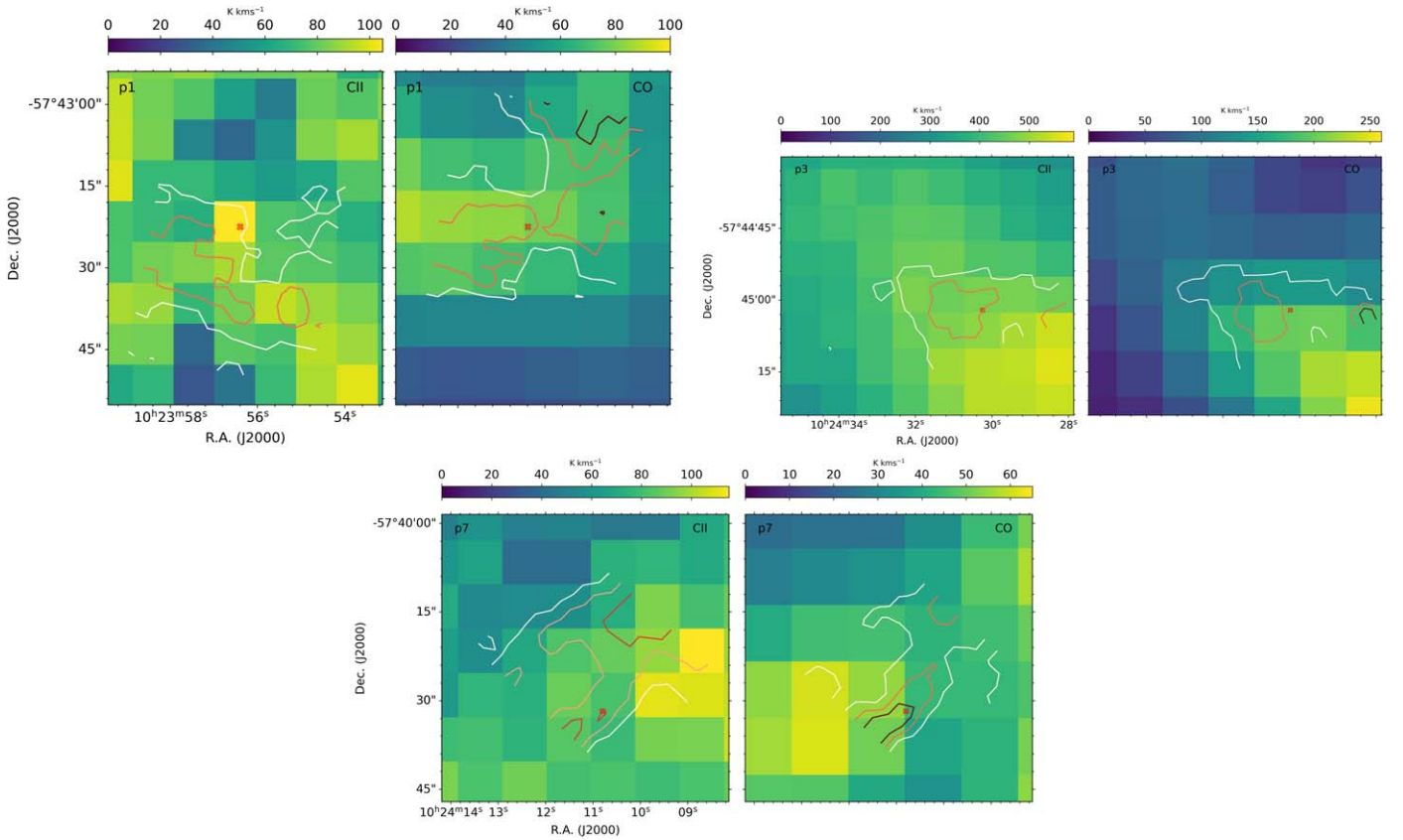


Figure 2. Emission maps of [C II] and ^{12}CO (3–2) toward the regions p1, p3, and p7 (shown in Figure 1). The [C II] maps are overlaid with H_2 0–0 $S(1)$ intensity contours, and the ^{12}CO maps are overlaid with H_2 0–0 $S(2)$ intensity contours. The contours are colored such that the darkest shade of red corresponds to the highest intensity. The red crosses mark the lines of sight for which the spectra are presented in Figure 3.

spans the velocity range -25 to 0 km s^{-1} and is most intense in the -12 to 0 km s^{-1} range. We have selected the “pillar,” as it may mark the radiative interaction of Wd2 with the ridge. However, while the pillar points back toward Wd2, we note that the Wolf-Rayet star WR20b is in close proximity and may have played a key role in its formation and in determining its physical conditions. While the above regions were selected based on morphological considerations of RCW 49, we have added three positions selected from the Spitzer IRS spectral survey also covered by the [C II], [O I], and ^{12}CO (3–2) surveys. Position “p1” (Figure 1, top left panel), marks the transition from the cavity surrounding Wd2 to the bright [C II] and $8 \mu\text{m}$ emission. Position “p3” overlaps with the eastern part of the ridge. Position “p7” is at the northern tip of the expanding shell identified by Tiwari et al. (2021).

4. Spatial Distribution of Observed Species

The northern cloud has bright [C II] and ^{12}CO emission but appears to be less prominent in GLIMPSE $8 \mu\text{m}$ emission (Figure 1). This is likely due to the high spectral resolution of the [C II] and ^{12}CO (3–2) observations, which allows us to disentangle the emission from this component (from 2 to 8 km s^{-1}) from the surroundings. Figure 1 shows bright [C II], ^{12}CO , and $8 \mu\text{m}$ emission toward the ridge. The shell is outlined very well by the [C II] and ^{12}CO emission as seen in Figure 1. However, unlike the [C II] emission distribution, the ^{12}CO emission distribution is fragmented toward the shell. This is also seen in the ^{13}CO emission map toward this region (Tiwari et al. 2021). For the $8 \mu\text{m}$ emission, similar to the

northern cloud, one cannot disentangle the emission solely from the shell owing to its lack of velocity resolution. Bright [C II], ^{12}CO , and $8 \mu\text{m}$ emission is observed toward the pillar.

The [C II] and ^{12}CO (3–2) emission maps overlaid with H_2 0–0 $S(1)$ and H_2 0–0 $S(2)$ emission contours, respectively, toward these positions are shown in Figure 2. Due to the lower velocity resolution $\Delta v \sim 500 \text{ km s}^{-1}$ in the IR line data, we compare their spatial distribution with the [C II] and ^{12}CO maps, where their emission is integrated over the entire velocity range. This ensures a fair comparison between the IR, FIR, and submillimeter wavelength data presented here. In general, the H_2 0–0 $S(1)$ emission distribution seems to be related more to the [C II] emission distribution than to the ^{12}CO emission distribution, and the H_2 0–0 $S(2)$ emission distribution seems to be related more to the ^{12}CO emission distribution than to the [C II] emission distribution. This suggests that the H_2 0–0 $S(1)$ line traces less dense gas compared to the H_2 0–0 $S(2)$ line. For p1, there are differences in the spatial distribution of the emission between H_2 0–0 $S(1)$ and H_2 0–0 $S(2)$. In p3, the H_2 , [C II], and ^{12}CO emission is brighter in the southwest, which is in the direction of the Wd2 cluster. In p7, the H_2 emission is essentially tracing the northernmost part of the shell. This structure is less detailed in the [C II] and ^{12}CO maps because of the lower angular resolution compared to the IR data. The dependence of the H_2 lines’ emission on the physical conditions can be seen in PDR model contour plots.¹¹ Along with the H_2 lines, several ionized gas tracers ([S IV] $10.5 \mu\text{m}$,

¹¹ See, e.g., https://dustem.astro.umd.edu/models/wk2006/h200s2s1_z1web.html.

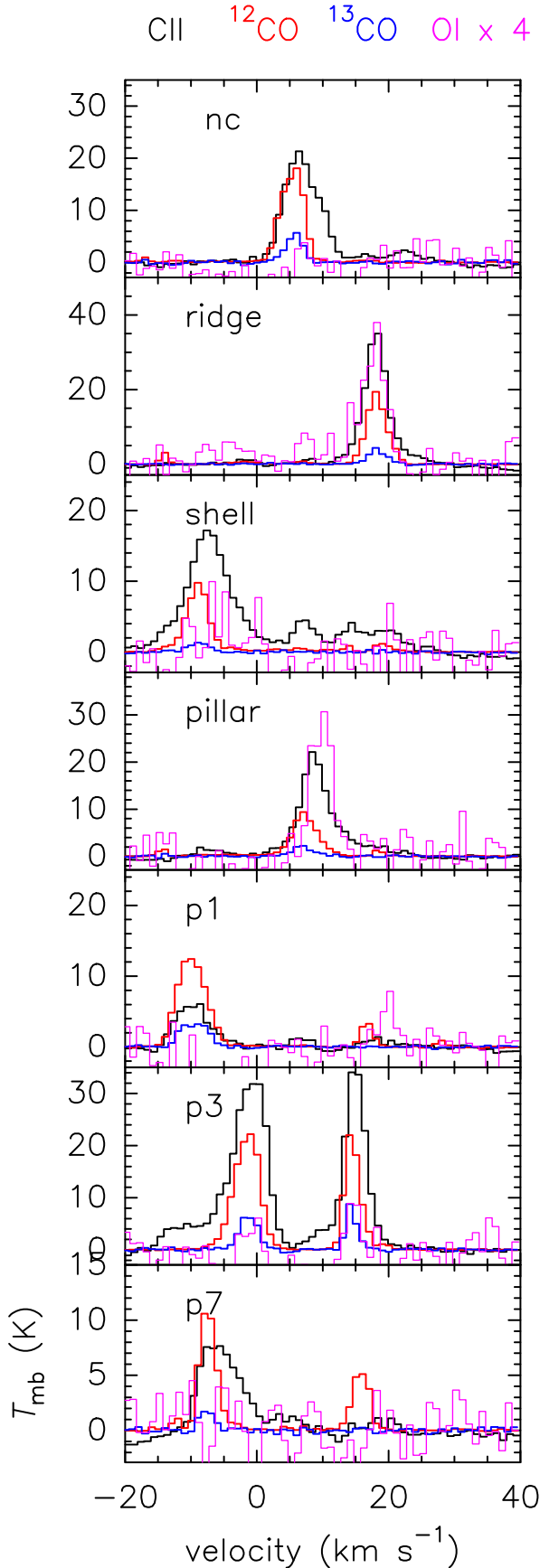


Figure 3. Representative spectra of [C II], ^{12}CO , ^{13}CO , and [O I] toward the northern cloud (nc), ridge, shell, pillar, p1, p3, and p7. All data were convolved to the same angular resolution of $\sim 20''$, and the spectral resolution of the spectra shown here is 1 km s^{-1} .

[Ne II] $12.8 \mu\text{m}$, [Ne III] $15.6 \mu\text{m}$, [S III] $18.7 \mu\text{m}$) were also mapped using the Spitzer telescope. Their corresponding IR spectra averaged over the regions of p1, p3, and p7 are discussed and shown in Appendix A and Figure 10, respectively.

5. Spectra

Figure 3 shows the representative spectra of the [C II], ^{12}CO , ^{13}CO , and [O I] $63 \mu\text{m}$ lines toward the seven regions analyzed in detail in this work.

We have convolved the maps to the same spatial resolution and extracted data for a single pixel. The similarity in peak position and profile of all tracers for positions, the ridge, p1, and the two velocity components in p3 ensures that we are tracing the same gas. However, for the northern cloud, shell, pillar, and p7, the velocity peak positions of the [C II] and [O I] lines are shifted by $\sim 1 \text{ km s}^{-1}$ with respect to the ^{12}CO line. These velocity shifts are in accordance with expectations for the advection of gas through the PDR (Tielens 2005), and we surmise that these species trace gas in the same PDR. In our source selection, we avoided clumps, which is vital for the PDR analysis described in Section 6.1. Though not used in our PDR analysis, we also present spectra of ^{13}CO toward the different regions. We can see that the ^{13}CO spectral profile follows that of ^{12}CO , suggesting no self-absorption in ^{12}CO from any cold foreground. Similarly, we did not observe any self-absorption features in the [O I] line profiles along the lines of sight where it was detected. This is in contrast with most [O I] observations toward other Galactic sources (Poglitsch et al. 1996; Liseau et al. 2006; Gerin et al. 2015; Rosenberg et al. 2015; Schneider et al. 2018; Goldsmith et al. 2021).

We considered the intensities integrated over the specific velocity ranges corresponding to their regions (same as shown in Figure 1). For the northern cloud and p1, the [O I] intensity values are upper limits to the [O I] emission toward these regions. For [C II], ^{12}CO , and [O I], they are estimated for the entire mapped regions by finding the rms noise in an emission-free velocity window. Their values are given in Table 1. Furthermore, there are also calibration uncertainties, which could be up to 10% for the ^{12}CO data (APEX, LASMA), $< 20\%$ for the [C II] data (SOFIA, upGREAT) and $\geq 20\%$ for the [O I] data.

6. PDR Diagnostics

We have used the PDR Toolbox¹² (Kaufman et al. 2006; Pound & Wolfire 2008, 2011), a Python-based software package that employs state-of-the-art PDR models to determine the physical conditions in PDRs (the FUV flux (G_0) and H nucleus density (n)) from observations.

In fitting the observations, we used the “Wolfire-Kaufman 2020 (wk2020)” model set. These are plane-parallel PDR models, with radiation that is incident on one side normal to the layer, that solve for the gas temperature in thermal equilibrium and atomic and molecular abundances in steady state. This model set has updated chemistry from that used in the Kaufman et al. (2006) models, most notably the chemical rates, PAH chemistry, and collision rates discussed in Hollenbach et al. (2012), Neufeld & Wolfire (2016), Kovalenko et al. (2018), Tran et al. (2018), and Dagdigan (2019), plus photodissociation

¹² <http://dustem.astro.umd.edu/>

Table 1
Observed and Model Intensity^a Values in Different Regions of RCW 49

Parameter	rms Noise	Northern Cloud	Ridge	Shell	Pillar	p1	p3	p3v1	p3v2	p7
R.A. (J2000)		10:23:59.7	10:24:06.5	10:24:29.7	10:24:11.7	10:23:56.2	10:24:30.3			10:24:11.1
Dec. (J2000)		−57:38:52.7	−57:46:17.2	−57:48:12.4	−57:49:06	−57:43:22.7	−57:45:02.5			−57:40:32.3
$I(\text{[C II]})$	0.18	6.7	9.9	9.4	11.0	3.0	34.0	20.0	12.0	4.2
$I(^{12}\text{CO (3–2)})$	0.003	0.032	0.029	0.017	0.017	0.028	0.076	0.047	0.029	0.014
$I(\text{[O I]})$	3.3	3.7	30.0	20.0	18.0	3.3	110.0	13.0	15.0	14.0
$I(\text{H}_2 \text{ 0–0 } S(1))$	0.05					0.31	1.6			1.0
$I(\text{H}_2 \text{ 0–0 } S(2))$	0.06					0.75	2.2			1.2
$I(\text{FIR})$		2400	12200	8200	5700	4200	12400			3800
$I_{\text{pre}}(\text{[C II]})$		4.0	6.2	5.5	4.6	6.6	5.9	4.7	5.6	10.0
$I_{\text{pre}}(^{12}\text{CO (3–2)})$		0.023	0.021	0.011	0.0082	0.039	0.014	0.013	0.014	0.031
$I_{\text{pre}}(\text{[O I]})$		11.0	24	14	8.7	67.4	17	11	17	110
$I_{\text{pre}}(\text{H}_2 \text{ 0–0 } S(1))$						0.79	0.34			0.220
$I_{\text{pre}}(\text{H}_2 \text{ 0–0 } S(2))$						0.16	0.022			0.75

Note.

^a All intensities are in units of $10^{-4} \text{ erg cm}^{-2} \text{ s}^{-1} \text{ sr}^{-1}$. The observed intensities were converted from $\text{K km s}^{-1} (\text{W})$ to $\text{erg cm}^{-2} \text{ s}^{-1} \text{ sr}^{-1} (I)$. For $[\text{C II}]$ $158 \mu\text{m}$, ^{12}CO (3–2), and $[\text{O I}]$ $63 \mu\text{m}$, respectively, the conversions are $I (\text{erg s}^{-1} \text{ cm}^{-2} \text{ sr}^{-1}) = 7.05 \times 10^{-6} \text{ W} (\text{K km s}^{-1})$, $4.238 \times 10^{-8} \text{ W} (\text{K km s}^{-1})$, and $1.1 \times 10^{-4} \text{ W} (\text{K km s}^{-1})$. I and I_{pre} are the observed intensities and intensities predicted by models, respectively. The columns p3, p3v1, and p3v2 correspond to the intensities integrated over the velocity window of -30 to 30 km s^{-1} , -15 to 5 km s^{-1} , and 5 to 20 km s^{-1} , respectively.

and photoionization rates in Heays et al. (2017), and collisional excitation rates for $[\text{O I}]$ in Lique et al. (2018). The models are carried out to a depth $A_V = 7$ with grain-surface chemistry turned off. We also adopt an incident (primary) cosmic-ray ionization rate per hydrogen $= 2.0 \times 10^{-16} \text{ s}^{-1}$ that decreases with depth as $1/N$ as suggested by Neufeld & Wolfire (2017). The PDR Toolbox uses the face-on line intensities that emerge from the PDR.

We used the $[\text{C II}]$, $[\text{O I}]$, and ^{12}CO (3–2) observations in the northern cloud, ridge, shell, and pillar. In addition to the above species, we used the H_2 0–0 $S(1)$ and H_2 0–0 $S(2)$ lines in p1, p3, and p7. The models take into account optical depth effects in the PDR. Moreover, we do not see any signature of self-absorption in our spectra (Figure 3) from a cold foreground. We convolved all the observations to the same angular resolution of ^{12}CO , which is $\sim 20''$. The observed line intensities are summarized in Table 1. As mentioned before, these values are toward specific lines of sight (see Figures 1 and 2).

6.1. Overlay Plots

Plotting overlays of intensity ratios of the observed species in the model space is a good way to understand the phase space (Figures 4 and 5) of allowable solutions. In such plots, locations where many observational lines cross indicate areas of (n, G_0) space that provide a good fit to the observations. For p1 and p7, we used the $[\text{C II}]$, $[\text{O I}]$, and ^{12}CO integrated intensities of the -15 to -5 km s^{-1} and the -12 to 0 km s^{-1} components, respectively, as these dominate the spectra (Figure 3) and the H_2 data. However, for p3, both -15 to 5 km s^{-1} and 5 – 20 km s^{-1} velocity components contribute significantly to the emission. Thus, we carried out the PDR analysis for p3 for three cases: first, where we used the integrated intensities of $[\text{C II}]$, $[\text{O I}]$, and ^{12}CO in the entire

velocity spread of -30 to 30 km s^{-1} , together with the H_2 emission; second, where we only used the integrated intensities of $[\text{C II}]$, $[\text{O I}]$, and ^{12}CO within the -15 to 5 km s^{-1} velocity range; and third, where, again, we only used the integrated intensities of $[\text{C II}]$, $[\text{O I}]$, and ^{12}CO within the 5 – 20 km s^{-1} velocity range. Moreover, we included ratios of the observed line intensities to the FIR continuum intensity. The FIR intensities were determined using the formalism described in Goicoechea et al. (2015), where the dust parameters (dust temperature and opacity) were calculated from 70 and $160 \mu\text{m}$ data from the Herschel Space Archive (HSA), obtained within the Hi-GAL Galactic plane survey (Molinari et al. 2010) observed with the Photodetector Array Camera and Spectrometer (PACS; Poglitsch et al. 2010). A detailed description of the method is given in Tiwari et al. (2021).

We used two complementary fitting techniques from the PDR Toolbox to estimate the radiation field and H density, G_0 and n . The first is the Levenberg–Marquardt least-squares fit (LSQ) method, which finds “best-fit” G_0 and n by minimizing the χ^2 of the observed intensity ratios versus the predicted model intensity ratios, weighted by the inverse square of the observational errors. The second method is a Markov Chain Monte Carlo (MCMC) method to determine the posterior probability density functions (PDFs) of G_0 and n . The MCMC results can be visualized through corner plots (Foreman-Mackey 2016), which display the PDFs of G_0 and n and the sampling distribution. As these distributions are approximately Gaussian, we characterize them on the overlay plots as 1σ contours in the estimated G_0 and n values for each region (Figures 4 and 5). As the estimated n and G_0 from the two methods are consistent, we report the values derived by the MCMC method.

Although all intensity ratios enter into the calculation of the physical parameters, the ratios with the smallest error bar (the

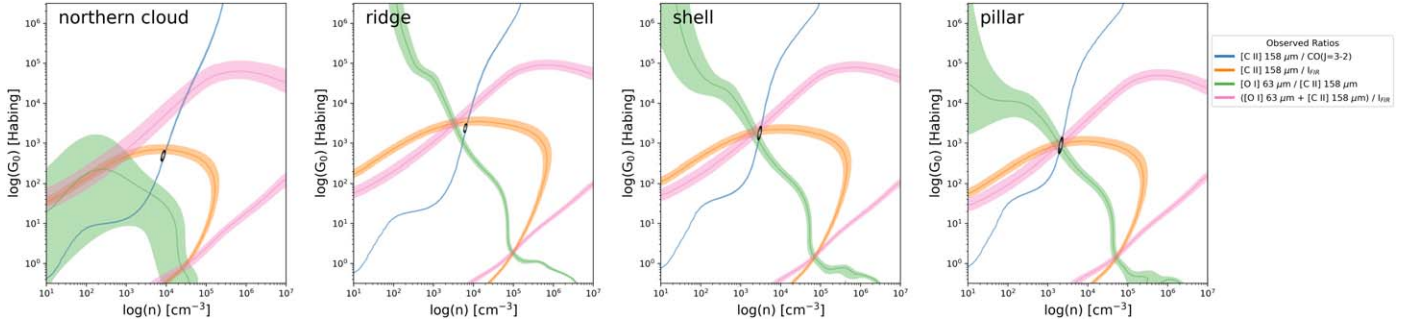


Figure 4. Overlay plots of the observed intensity ratios in the PDR Toolbox modeled grid of G_0 and n for the northern cloud, ridge, shell, and pillar. The shaded region corresponds to the error on the observations. Each plot is overlaid with the contours of its corresponding corner plot.

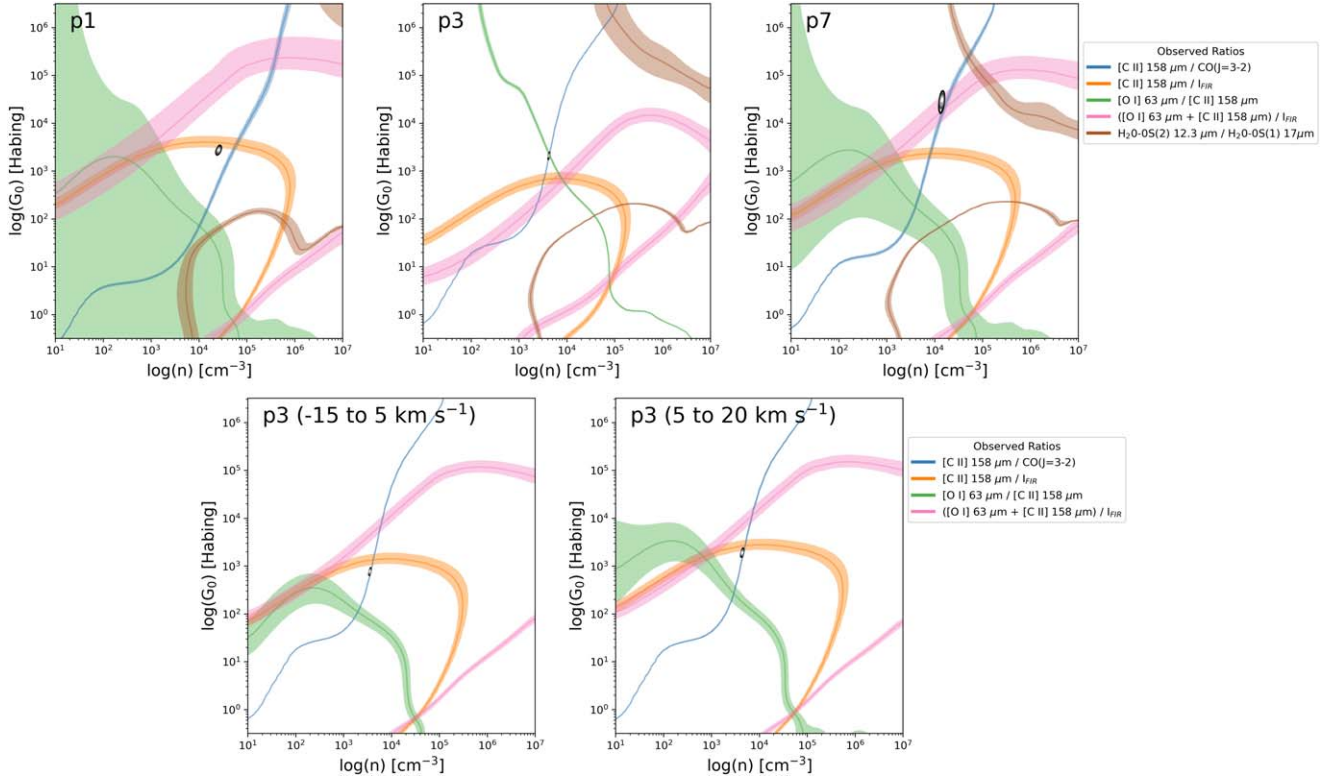


Figure 5. Overlay plots of the observed intensity ratios in the PDR Toolbox modeled grid of G_0 and n for p1, p3 (top and bottom panels include and exclude H_2 data, respectively), and p7. The shaded region corresponds to the error on the observations. Each plot is overlaid with the contours of its corresponding corner plot.

thinnest curve in overlay plots) dominate the fits. It can be seen in Figures 4 and 5 that the $[C II]/CO$ ratio plays the most important role in determining the physical conditions for different regions. In addition, in certain cases, two points of intersection exist, but the $[C II]/CO$ dominates the determination of the physical conditions. The results are summarized in Table 2.

6.2. Temperatures and Pressures

Using the derived n and G_0 values for different regions, we determined the PDR surface temperatures (T_{surf} from the T_{surf} map in the PDR Toolbox), which are the model gas temperatures at $A_V = 0.01$ and are characteristic of the $[C II]$ and $[O I]$ emitting regions (Table 2). We also estimated the $[C II]$ excitation temperatures (T_{ex}) assuming an optical depth of ~ 3 , which should be considered an upper limit for the entire mapped region of RCW 49 (Tiwari et al. 2021). The calculated

T_{ex} ($[C II]$) are given in Table 2. It can be seen that the T_{ex} ($[C II]$) values are less than the T_{surf} values. This could be because $[C II]$ is actually optically thin toward most of the lines of sight and a derivation assuming it to be optically thick results in lower excitation temperatures. Alternatively, a low excitation temperature may indicate a density below the critical density.

We also calculated thermal (p_{th}) and turbulent (p_{turb}) pressures (Table 2) in the different regions of RCW 49 using

$$p_{\text{th}} = nT_{\text{surf}} (\text{K cm}^{-3}) \quad (1)$$

and

$$p_{\text{turb}} = \mu mn \left[\frac{\Delta v_{\text{turb}}^2}{8 \ln(2)k} \right] (\text{K cm}^{-3}), \quad (2)$$

Table 2
Derived Physical Parameters in Different Regions of RCW 49

Parameter	Units	Northern Cloud	Ridge	Shell	Pillar	p1	p3	p3v1	p3v2	p7
n	10^3 cm^{-3}	8.6(0.5)	6.4(0.35)	3.1(0.2)	2.2(0.1)	27.0(2.0)	4.3(0.1)	3.6(0.1)	4.5(0.2)	14.0(1.0)
G_0	10^3 Habing units	0.5(0.07)	2.4(0.3)	1.9(0.4)	0.97(0.21)	2.9(0.32)	2.1(0.2)	0.79(0.07)	2.0(0.2)	32.0(8.0)
$G_0(\text{FIR})$	10^3 Habing units	0.92	4.7	3.2	2.2	1.7	4.8			1.5
T_{surf}	K	160	246	250	223	244	242	196	242	441
$T_{\text{ex}}([\text{C II}])$	K	55.2	72.0	47.3	54.6	33.6		70.4	73.0	36.8
p_{th}	10^6 K cm^{-3}	1.4	1.6	0.77	0.5	6.6	1.0	0.71	1.1	6.2
p_{turb}	10^6 K cm^{-3}	9.4	3.0	3.5	1.8	25.0	12.0	3.9	1.8	19.0
Δv_{turb}^2	$\text{km}^2 \text{ s}^{-2}$	38.5	16.7	39.9	29.3	32.1	101.4	38.1	14.2	48.4
$N_{\text{H}}(160 \mu\text{m})$	10^{22} cm^{-2}	4.5	3.3	5.6	4.2	4.5		13.0	13.0	4.6
$N_{\text{H}}(^{13}\text{CO})$	10^{22} cm^{-2}	1.3	0.84	0.36	0.78	1.3		1.6	1.3	0.4

Note. Parameter n is hydrogen volume density, and G_0 is the FUV flux determined from the PDR Toolbox. Errors from fits are in parentheses. $G_0(\text{FIR})$ is the FUV flux determined from the Herschel data. $T_{\text{ex}}([\text{C II}])$ is the [C II] excitation temperature. Parameters p_{th} and p_{turb} are the thermal and turbulent pressures, respectively. Δv_{turb}^2 is the turbulent velocity in $\text{km}^2 \text{ s}^{-2}$. $N_{\text{H}}(160 \mu\text{m})$ and $N_{\text{H}}(^{13}\text{CO})$ are hydrogen column densities estimated using the 160 μm Herschel data and the ^{13}CO APEX data, respectively. The columns p3, p3v1, and p3v2 correspond to the intensities integrated over the velocity windows of -30 to 30 km s^{-1} , -15 to 5 km s^{-1} , and 5 – 20 km s^{-1} , respectively.

where

$$\Delta v_{\text{turb}}^2 = \Delta v_{\text{FWHM}}^2 - [8 \ln(2) k T_{\text{surf}} / m_{\text{c}}]. \quad (3)$$

Here n is density (values from Table 2), T_{surf} is surface temperature (values in Table 2), $\mu = 1.3$ is the mean molecular weight, m is the hydrogen mass, Δv_{FWHM} is the FWHM line width of [C II] emission spectra (shown in Figure 3 and summarized in Table 2), k is the Boltzmann constant, and m_{c} is the carbon atom’s mass. For determining p_{turb} , we assumed Δv_{turb}^2 to be dominated by turbulence. However, the broad line widths of [C II] could also be affected by velocity crowding along a line of sight. Thus, the p_{turb} estimated here should be considered as upper limits.

We can see that the turbulent pressures are higher than the thermal pressures and thus dominate the dynamics of the gas in all regions of RCW 49. This is similar to the findings toward the stellar-feedback-driven shells of RCW 49 and RCW 36 (Tiwari et al. 2021; Bonne et al. 2022). When comparing the p_{th} and p_{turb} values derived for the shell in this work with those from Tiwari et al. (2021), we find that the values estimated here are lower by up to a factor of ~ 1.6 . This difference is because in Tiwari et al. (2021) we derived the physical parameters using the average intensity values of [C II] and ^{12}CO toward the entire shell of RCW 49, while in this work we used the observed intensity values of [C II], [O I], ^{12}CO , and FIR toward a specific line of sight. Another reason is that in Tiwari et al. (2021) the G_0 values toward the shell were estimated using the synthetic spectra for the stellar population of RCW 49 using the PoWR stellar atmosphere grids (Sander et al. 2015), while in this work we used the PDR Toolbox to derive G_0 values. In addition, the PDR models we used in this work are newly updated (“wk2020”) compared to the “wk2006” models used in Tiwari et al. (2021).

6.3. Hydrogen Nucleus Column Densities

We estimated the dust column densities toward different regions of RCW 49 from the dust spectral energy distribution (see Tiwari et al. 2021 for details). The derived dust optical depths are converted to N_{H} (Table 2) using the Draine (2003) $R_{\text{V}} = 3.1$ value of the dust extinction cross section per

hydrogen nucleus at $160 \mu\text{m}$. We also calculated N_{H} using the ^{13}CO data toward the same lines of sight. We first estimated the excitation temperature using the optically thick ^{12}CO data, which can then be used to determine ^{13}CO optical depths. Finally, using the ^{13}CO integrated intensities along with the excitation temperatures and optical depths, we estimated the ^{13}CO column densities, which can be converted to H_2 column densities (Table 2), adopting a $\text{H}_2/^{13}\text{CO}$ abundance of 6.1×10^5 (Milam et al. 2005; Tielens 2005). The column densities derived from the dust are in general higher than the ones derived from ^{13}CO . This may indicate the presence of CO-dark gas along the line of sight. Alternatively, column density estimation from 70 and $160 \mu\text{m}$ data can include foreground and background contribution of up to 30% (Tiwari et al. 2021).

6.4. Phase-space Diagrams

To examine the dispersion in physical properties across the mapped regions, we extracted all the data points from the [C II], CO, [O I], and FIR intensity maps and overlaid their ratios on the n and G_0 modeled phase space (Figures 6 and 7). These specific diagnostic plots were selected for this analysis because the line ratios involved separate out n and G_0 reasonably well into orthogonal directions. Specifically, the [C II]/CO (3–2) and the [C II]/FIR ratios are sensitive to G_0 , while the [C II]/[O I] and ([O I] + [C II])/FIR probe n . These diagnostic plots allow us to generalize the results of the detailed analysis of the specific points in Section 6.1 to the whole region.

All the data were regridded to the same angular resolution of $\sim 20''$ and filtered such that only data with values $> 3\sigma$ are included. For [C II] and CO, most of the data points had values $> 3\sigma$. However, for [O I], the number of such data points decreased owing to lower sensitivity; thus, we used upper limits in certain cases.

The individual points in these regions cover a wide range in n and G_0 (Table 3). The estimated range of G_0 values derived from ratios using [C II], ^{12}CO , and FIR intensities is similar to those derived using [C II], [O I], and FIR intensities. However, the estimated n values differ in certain cases. Specifically, in p1, the n values in the left panel are higher by almost 2 mag compared to those in the right panel. There are also significant

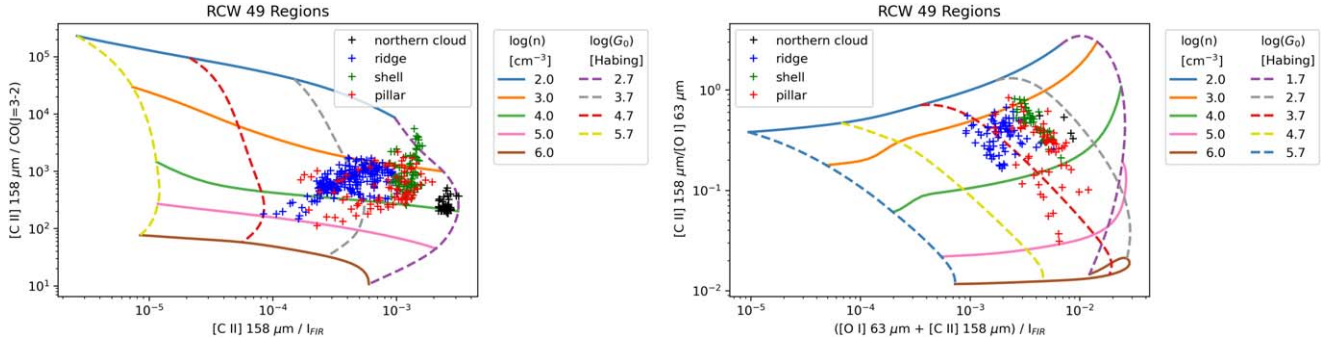


Figure 6. The n and G_0 model phase space for [C II], [O I], ^{12}CO , and FIR intensities. Left panel: modeled phase space with respect to [C II]/CO (3–2) vs. [C II]/FIR. Right panel: modeled phase space with respect to [C II]/[O I] vs. [O I] + [C II]/FIR. Data points are shown with colored (different regions) markers. The solid and dashed colored curves depict constant n and G_0 values, respectively.

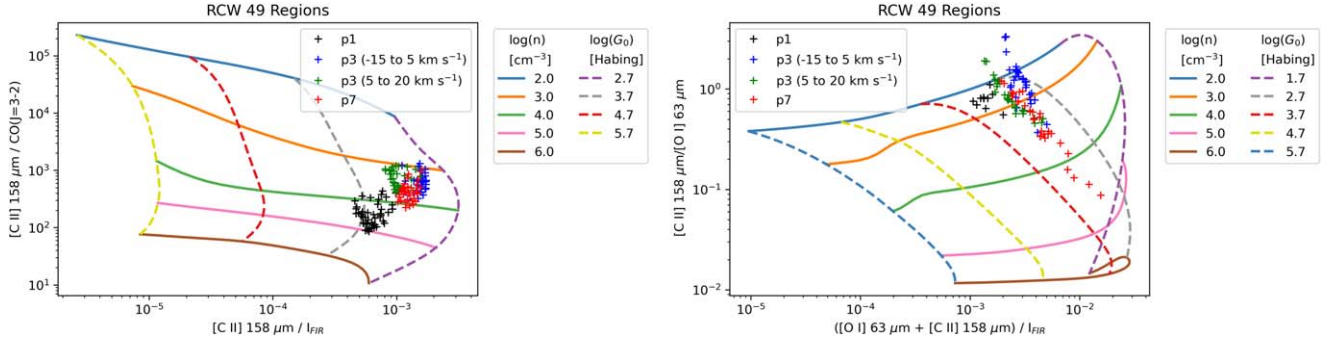


Figure 7. The n and G_0 model phase space for [C II], [O I], ^{12}CO , and FIR intensities. Left panel: modeled phase space with respect to [C II]/CO (3–2) vs. [C II]/FIR. Right panel: modeled phase space with respect to [C II]/[O I] vs. [O I] + [C II]/FIR. Data points are shown with colored (different regions) markers. The solid and dashed colored curves depict constant n and G_0 values, respectively.

Table 3
Physical Conditions Estimated by Phase-space Diagrams

Parameter	Units	Northern Cloud	Ridge	Shell	Pillar	p1	p3v1	p3v2	p7
n ([C II]–CO–FIR)	10^3 cm^{-3}	5–10	1–100	0.5–5	1–100	10–100	1–10	1–10	1–10
n ([C II]–[O I]–FIR)	10^3 cm^{-3}	5–7	1–10	1–10	1–100	0.1–1	0.5–5	0.5–5	0.1–70
G_0 ([C II]–CO–FIR)	10^3 Habing units	0.5–0.7	1–50	0.5–1	1–10	0.8–6	0.6–0.7	1	0.7–1
G_0 ([C II]–[O I]–FIR)	10^3 Habing units	0.5–0.7	3–10	1	0.7–10	1–4	0.6–1	1	1

Note. Parameters with [C II]–CO–FIR correspond to the values estimated from the left panels of Figures 6 and 7. Similarly, parameters with [C II]–[O I]–FIR correspond to the values estimated from the right panels of Figures 6 and 7.

differences in the ridge and p7. This is most likely because of the lower sensitivity of the [O I] data toward these regions, resulting in a bias toward higher-density regions.

7. Discussion

7.1. Overlay Plots versus Phase-space Diagrams

In Section 6.1 we used the LSQ and MCMC methods to find the best point of intersection of all the observed ratios in different positions of RCW 49, while in Section 6.4 we used phase-space diagrams on a modeled grid of different combinations of ratios of [C II], [O I], ^{12}CO , and FIR intensities. Although the phase-space diagrams are a good way to visualize the entire data (~ 30 – 230 [C II] and ^{12}CO spectra and ~ 3 – 70 [O I] spectra for different regions) in n – G_0 space and also visualize gradients in a specific region, the estimations are biased based on the combination of ratios used for specific species. For instance, the [C II]/CO (3–2) ratio is more

sensitive to G_0 , while the [O I]/[C II] ratio is more sensitive to n . Another point to note is that observed [O I] observations have lower sensitivity than the other tracers, and thus the phase space probed by the [O I]/[C II] ratio will have larger errors compared to the phase space probed by the [C II]/CO (3–2) ratio. In contrast, deriving the physical parameters using all the ratios (four in Figure 4 and five in Figure 5) simultaneously toward a representative position in different regions (as done in Section 6.1) should be considered a more accurate approach for PDR analysis. Another way to compare the physical parameters derived from the overlay plots and the phase-space diagrams is by identifying the specific data points used in the overlay plots (from Figures 4 and 5) in the phase-space diagrams. These figures are shown and discussed in detail in Appendix B and in Figures 11 and 12. We find that the data points used to do the analysis of the overlay plots lie on the extreme ends of the phase space probed by the entire data sets of different regions, which might imply that the results obtained from the overlay

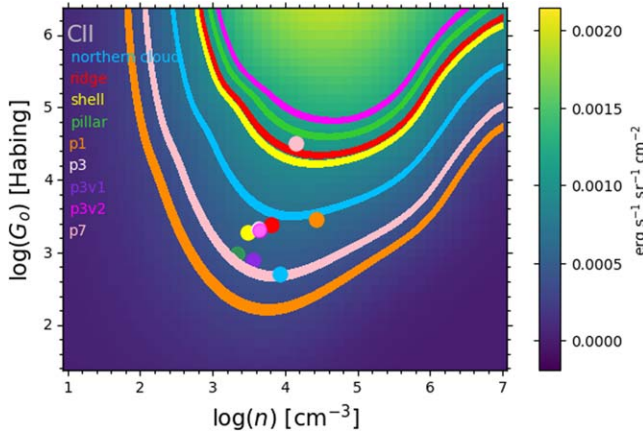


Figure 8. [C II] modeled intensity map as a function of G_0 and n . The map is highlighted with the observed intensity contours, as well as marked with the model-predicted intensity values for different regions in different colors. The thickness of the contours corresponds to their observational error bars.

plots are not characteristic of the entire regions. However, as mentioned in Section 5, these specific lines of sight were chosen for the overlay plots to ensure that clump emission is excluded, which can interfere with the PDR analysis and give misleading results. Thus, we believe that the overlay plots (results summarized in Table 2) toward these representative lines of sight are a better way to estimate the physical parameters, and we use them as a guide to understand stellar feedback in RCW 49.

7.2. Observed versus Model Intensities

As described in Section 6.1, the PDR Toolbox derives n and G_0 (given in Table 2) from the ratios of [C II], [O I], CO (3–2), H₂ 0–0 $S(1)$, H₂ 0–0 $S(2)$, and FIR intensities. We will now compare the individual observed intensity values of different species with those predicted by the models. For this, we extracted the intensity values of [C II], CO, [O I], H₂ 0–0 $S(1)$, and H₂ 0–0 $S(2)$ from the “wk2020” PDR Toolbox models for the derived n and G_0 values for different regions. We can see from Table 1 that the model-predicted intensity values of different species differ from their observed values. The differences are most significant for p3 and p7 positions.

These differences can be visualized in Figure 8, where the [C II] modeled intensity map is highlighted with the observed intensity contours, along with the predicted [C II] intensities for different regions in RCW 49. It is clear that the observational errors do not explain the difference between the predicted and observed [C II] intensity values.

We ascribe these differences to the effects of geometry. The current PDR models assume a face-on geometry, and we can check results for an edge-on geometry (see Pabst et al. 2017). In this view, the radiation is incident from the side, and the PDR layers are spread across the sky, with the atomic gas closest to the incident radiation and the molecular gas at greater distance. We calculate the line intensities from the (face-on) local emissivities integrated along the line of sight while accounting for the line optical depths. At a typical radiation field and density found in Table 2 ($G_0 \sim 3 \times 10^3$ Habing units and $n \sim \times 10^3 \text{ cm}^{-3}$), the [C II] intensity is about a factor of 2 higher in the edge-on case compared to face-on owing to the increased column density along the line of sight. The [O I] and ¹²CO lines are relatively unchanged since they are already

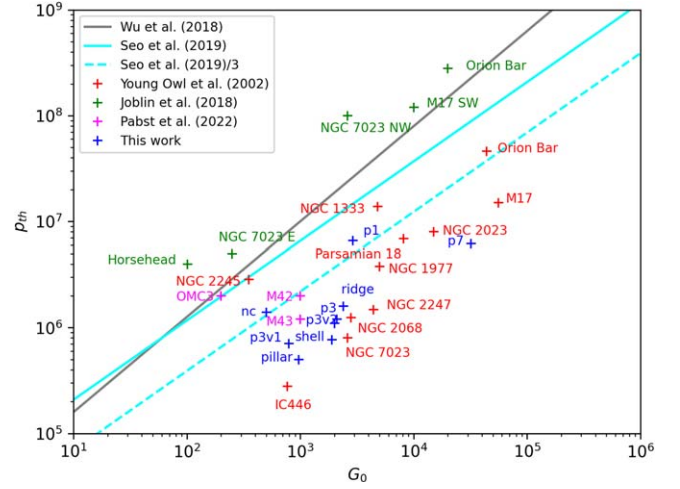


Figure 9. p_{th} vs. G_0 for different regions. The red, green, magenta, and dark-blue points correspond to regions studied by Young Owl et al. (2002; using FIR line analysis), Joblin et al. (2018; using high- J ¹²CO analysis), Pabst et al. (2022; using low- J ¹²CO and [C II] analysis), and this work, respectively. p3v1 and p3v2 correspond to the two velocity components of p3: -15 to 5 km s^{-1} and 5 – 20 km s^{-1} , respectively. The black line refers to the fit by Wu et al. (2018) using mid- to high- J ¹²CO and [C I] analysis. The light-blue solid and dashed lines are for the analytic relation by Seo et al. (2019) and the relation divided by 3 to account for pressure equipartition, respectively.

optically thick and increasing the column density does little to increase the emitted line intensity. However, this would lead to disagreement with the observed intensity ratios. Since the density is greater than the [C II] critical density but less than the [O I] and ¹²CO critical densities, an increase in the density by a factor of 2 does little to change [C II] but increases [O I] by a factor of ~ 2 and ¹²CO by a factor of ~ 2 – 3 . Combining these two effects, the observed ratios can be explained by an edge-on model with a factor of ~ 2 higher density. Thus, the model fits to some of the regions could be improved, and geometry introduces an uncertainty by a factor of ~ 2 in density. Position p3 remains problematic with a high observed [C II] intensity. Such high intensities $>10^{-3} \text{ erg cm}^{-2} \text{ s}^{-1} \text{ sr}^{-1}$ typically indicate a large contribution from ionized gas along the line of sight (Seo et al. 2019).

Overall, we believe that geometrical effects are the main cause for the difference between the predicted and the observed intensity values for various species.

7.3. Relationship between p_{th} and G_0

We studied the relationship between p_{th} and G_0 for different regions of RCW 49 (Table 2) and for various PDRs studied in the literature. Figure 9 is adapted from Figure 20 in Pabst et al. (2022). We can see that all studies follow the general trend, where p_{th} increases with G_0 . However, studies by Young Owl et al. (2002; red data points in Figure 9) and Joblin et al. (2018; green data points in Figure 9) are somewhat shifted when compared to the regions of RCW 49 owing to higher G_0 and p_{th} values, respectively. Young Owl et al. (2002) estimated higher values of G_0 for their sources compared to the values determined by Salgado et al. (2016), Joblin et al. (2018), and Pabst et al. (2022). Joblin et al. (2018) used high- J ¹²CO lines for their analysis and therefore probe high-density gas and/or clumps owing to the high critical densities of these lines. The relation between p_{th} and G_0 as derived by Wu et al. (2018;

black line in Figure 9) is also derived from high- J ^{12}CO line analysis and is biased toward high-density clumps.

There is a simple relation (shown with a solid light-blue line in Figure 9) between p_{th} and G_0 for a PDR in pressure equilibrium within a Strömgren sphere (Young Owl et al. 2002; Seo et al. 2019). The different regions of RCW 49 (dark-blue data points in Figure 9) lie close to the above analytical relation, taking equipartition of thermal, turbulent, and magnetic pressures into account. This is similar to the sources studied by Pabst et al. (2022). Thus, the physical conditions in different regions of RCW 49 are in agreement with the basic Strömgren relation for an H II region.

7.4. Impact of Stellar Feedback on Different Regions

In this section, we compare different regions of RCW 49 based on the derived physical conditions. The derived physical conditions in the seven regions of RCW 49 are indicative of different effects of stellar feedback on these regions. As justified earlier, we use the analysis reported in Section 6.1 for the comparison. We compare the regions p1, p3, and p7 separately from the northern cloud, ridge, shell, and pillar because analysis of the former includes H_2 emission along a line of sight, while analysis of the latter excludes H_2 emission and includes emission only from specific velocity components corresponding to the given structure.

For G_0 values, the different regions can be placed in an increasing order: northern cloud with the lowest G_0 , followed by the pillar, shell, and ridge with the highest G_0 . Similarly, for the density, we can place the different regions in an increasing order: pillar with the lowest n , followed by the shell, ridge, and northern cloud with the highest n .

The northern cloud is located farthest from the Wd2 cluster, which is likely the reason that it has the lowest G_0 of the regions studied. The ridge, which is ~ 40 pc away from the northern cloud (Furukawa et al. 2009), is closest to the Wd2 cluster, corresponding to the highest G_0 value. Moreover, Furukawa et al. (2009) suggested that the northern cloud and the ridge collided ~ 4 Myr ago, forming the Wd2 cluster (age $\sim 2\text{--}3$ Myr; Furukawa et al. 2009; Tiwari et al. 2021). The compression associated with this collision may be the cause for the higher densities derived for these regions. The high density of the ridge is also consistent with the ongoing star formation reported in it (Whitney et al. 2004; Tiwari et al. 2021). In addition, the derived densities of the northern cloud and the ridge in this work are similar to the ones $((3\text{--}8) \times 10^3 \text{ cm}^{-3})$ derived by Ohama et al. (2010) using the large-velocity gradient analysis of molecular emission lines. The mechanical feedback of the Wd2 cluster drives the expanding (at $\sim 13 \text{ km s}^{-1}$) shell of RCW 49, which is ~ 6 pc from the cluster. A secondary (younger and lower in mass) generation of star formation is taking place in the shell of RCW 49 (as discussed in Whitney et al. 2004; Tiwari et al. 2021). The pillar has similar n and G_0 values (1.5 and 1.6 times lower) to the shell. From the pillar's morphology, it seems to be created by the Wd2 cluster. However, it also has the Wolf-Rayet star, WR20b, relatively closer to it, and that could also be responsible for illuminating the pillar. Currently, we are unable to quantify the effects of radiative feedback from WR20b in defining the physical conditions of the pillar. But comparing the masses and bolometric luminosities of WR20b with those of the Wd2 cluster, the stellar (radiative and mechanical)

feedback from WR20b should be not more than 20% of that from Wd2.

Among p1, p3, and p7, p7 has the highest G_0 value, while the -15 to 5 km s^{-1} velocity component of p3 has the lowest G_0 value. p1 has the highest n value, and again the -15 to 5 km s^{-1} velocity component of p3 has the lowest n value. p7 is the northernmost part of the shell of RCW 49, and in the west of it, the shell gets broken. We also located an early-type O9V star close to this line of sight. Thus, the high G_0 value in p7 could be due to its proximity to this star. p1 is closest to the Wd2 cluster and has dense gas toward it (bright ^{12}CO and $870 \mu\text{m}$ emission), suggesting the possibility of triggered star formation in its early stage. Toward position p3, we see a superposition of the shell (-15 to 5 km s^{-1}) and the ridge ($5\text{--}20 \text{ km s}^{-1}$) components. The G_0 values for the shell component are lower than those of the ridge. This can be explained by their location with respect to the Wd2 cluster. As mentioned in the previous paragraph, the ridge is close to Wd2, while the shell is about 6 pc away from it. The ridge component is also denser compared to the shell component in p3, which is consistent with its ongoing star formation.

8. Conclusions

We studied seven different regions of RCW 49 using the [C II], [O I], ^{12}CO (3–2), H_2 0–0 $S(1)$, and H_2 0–0 $S(2)$ observations. Four of these regions, the northern cloud, ridge, shell, and pillar, have the [C II], [O I], and ^{12}CO (3–2) data toward them observed through the FEEDBACK program. These regions are both spatially and spectrally distinct. The other three regions, p1, p3, and p7, have the H_2 0–0 $S(1)$ and H_2 0–0 $S(2)$ data observed by the Spitzer telescope in addition to the FEEDBACK data. We presented the [O I] and H_2 data (spectra and emission maps) toward RCW 49 for the first time in this paper. We found that the H_2 0–0 $S(1)$ emission distribution follows that of [C II], while the H_2 0–0 $S(2)$ emission distribution follows that of CO, indicating that H_2 0–0 $S(2)$ arises from a denser gas compared to H_2 0–0 $S(1)$ in RCW 49.

To determine the physical conditions in different regions of RCW 49, we compared our observations with the updated PDR models. We justified that the PDR analysis done using the overlay plots and data fits is a better technique than using phase-space diagrams to derive the physical conditions in the ISM. Based on the physical conditions, we studied the effects of stellar feedback on the evolution of different regions in RCW 49. We found that the ridge (closest to Wd2) has the highest G_0 value, while the northern cloud (farthest from Wd2) has the lowest G_0 . However, both the northern cloud and the ridge have high densities, which is consistent with previous studies, suggesting that these regions are part of large-scale clouds, whose collision led to the formation of the Wd2 cluster. In addition, there is evidence of ongoing star formation in the ridge. Among p1, p3, and p7, p1 has the highest density, and based on the bright ^{12}CO and $870 \mu\text{m}$ emission toward it, we suggest early-stage star formation in this region. p7 has the highest FUV flux, and this is attributed to the impinging radiation from an early-type O9V star close to this position.

We also estimated pressures toward these regions and found that the p_{turb} dominate (when compared to p_{th}) the dynamics of the gas in RCW 49. Furthermore, the observed relationship between p_{th} and G_0 follows the theoretical relationship derived

from the Strömgren relation for an H II region, which has also been observed toward several other PDRs.

We would like to thank the referee for their constructive comments and helping to clarify the paper.

This study was based on observations made with the NASA/DLR Stratospheric Observatory for Infrared Astronomy (SOFIA). SOFIA is jointly operated by the Universities Space Research Association, Inc. (USRA), under NASA contract NNA17BF53C, and the Deutsches SOFIA Institut (DSI), under DLR contract 50 OK 0901 to the University of Stuttgart. upGREAT is a development by the MPI für Radioastronomie and the KOSMA/University of Cologne, in cooperation with the DLR Institut für Optische Sensorsysteme.

Financial support for the SOFIA Legacy Program, FEEDBACK, at the University of Maryland was provided by NASA through award SOF070077 issued by USRA. M.W.P. acknowledges support for development of the PDR Toolbox from NASA ADAP No. 80NSSC19K0573.

The FEEDBACK project is supported by the BMWI via DLR, project No. 50 OR 1916 (FEEDBACK). N.S., R.S., and L.B. acknowledge support by the Agence National de Recherche (ANR/France) and the Deutsche Forschungsgemeinschaft

(DFG/Germany) through the project “GENESIS” (ANR-16-CE92-0035-01/DFG1591/2-1).

This work was partly supported by the Collaborative Research Centre 956, funded by the DFG.

Appendix A IR Spectra

Figure 10 displays the average spectra in a $\sim 10\text{--}20\ \mu\text{m}$ wavelength window toward p1, p3, and p7. H₂ lines are brightest in p3 by $\sim 1.5\text{--}3$ times compared to p1 and p7. This is similar to our [C II], [O I], and ¹²CO emission, which is brightest toward the ridge. The H₂ 0–0 S(1) line is similarly intense in p1 and p7; however, the H₂ 0–0 S(2) line is ~ 2 times brighter in p1 than in p7. This can be attributed to the fact that p1 is closer to Wd2 than p7 and is thus exposed to stronger radiation to heat the gas and excite the H₂ 0–0 S(2) line, which has a higher upper-level energy.

For the ions, [Ne II] and [S III] are brightest in p3 and least bright in p7. This is similar to the H₂ lines. However, the relatively more ionized lines of [Ne III] and [S IV] are brightest in p1 and least bright in p7. This can again be explained because of the location of these regions with respect to Wd2: p1 is closest and p7 is farthest.

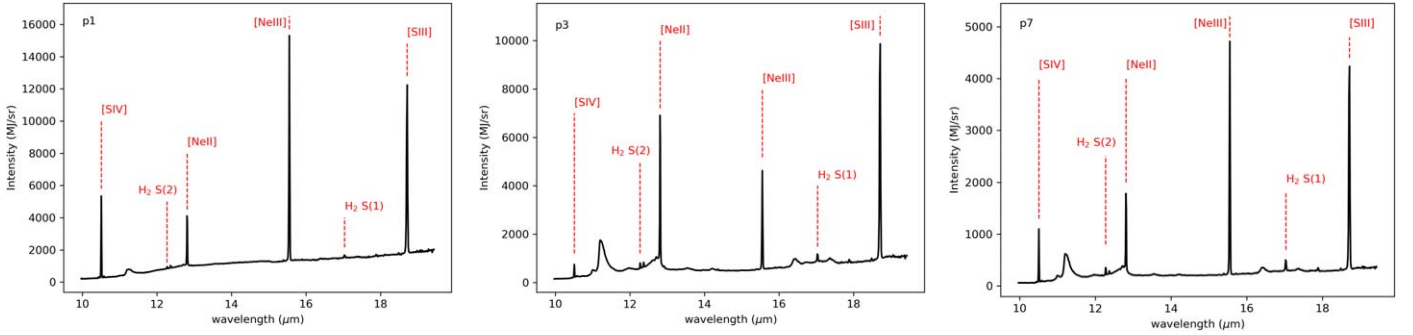


Figure 10. Average IR spectra toward p1, p3, and p7 (regions shown in Figure 1). The six species presented in this work are marked with red dashed lines.

Appendix B

Phase-space Diagrams for Specific Data Points

Figures 11 and 12 show phase-space diagrams overlaid with specific data points (colored crosses) selected for the PDR analysis presented in Section 6.1 and Figures 4 and 5. These data points mostly lie close to the boundaries of the shaded areas (corresponding to the space probed by the entire data sets for different regions) in the phase-space diagrams. For instance, in the

left panel of Figure 11, the data points used to make the overlay plot for the ridge and pillar are probing lower values of G_0 compared to its shaded area, while for the shell it is probing a higher value of G_0 . Moreover, the data point corresponding to the pillar in the right panel of Figure 11 is probing a lower value of n compared to its shaded area. Another clear example can be seen in the right panel of Figure 12, where the data point corresponding to p7 probes lower density compared to its shaded area.

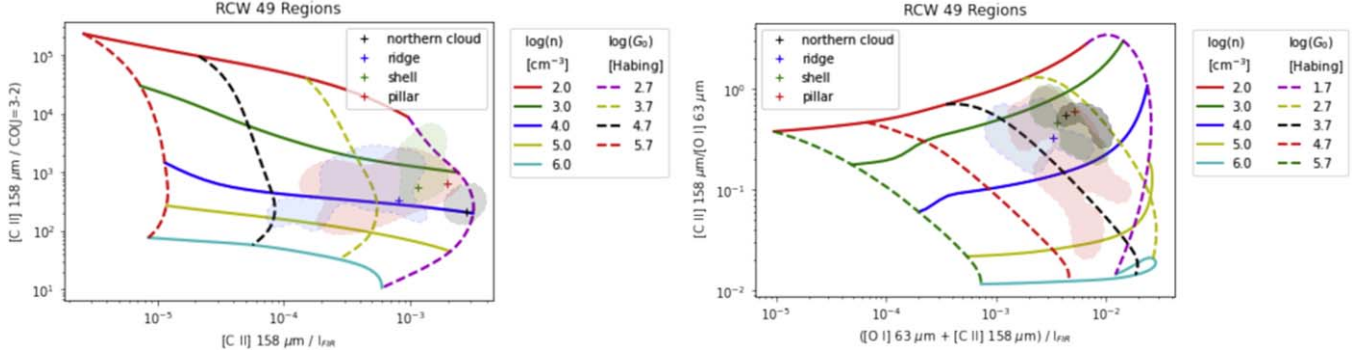


Figure 11. The n and G_0 model phase space for $[C II]$, $[O I]$, ^{12}CO , and FIR intensities. Left panel: modeled phase space with respect to $[C II]/CO(3-2)$ vs. $[C II]/FIR$. Right panel: modeled phase space with respect to $[C II]/[O I]$ vs. $[O I] + [C II]/FIR$. Data points are shown in colored (different regions) markers. The shaded regions correspond to the spread in the phase space as probed by the entire data set toward different regions as shown in Figure 6. The solid and dashed colored curves depict constant n and G_0 values, respectively.

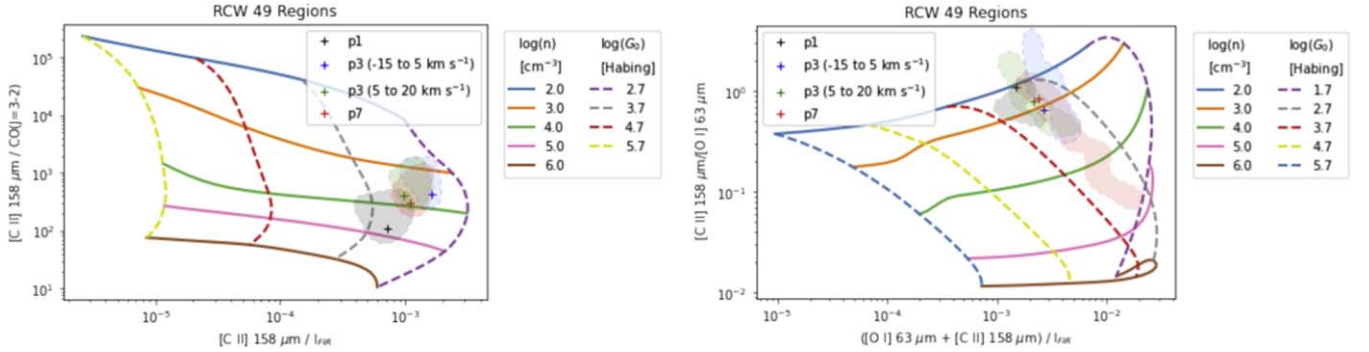


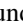
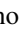











Figure 12. The n and G_0 model phase space for $[C II]$, $[O I]$, ^{12}CO , and FIR intensities. Left panel: modeled phase space with respect to $[C II]/CO(3-2)$ vs. $[C II]/FIR$. Right panel: modeled phase space with respect to $[C II]/[O I]$ vs. $[O I] + [C II]/FIR$. Data points are shown with colored (different regions) markers. The shaded regions correspond to the spread in the phase space as probed by the entire data set toward different regions as shown in Figure 7. The solid and dashed colored curves depict constant n and G_0 values, respectively.

ORCID iDs

M. Tiwari  <https://orcid.org/0000-0003-4260-2950>
 M. Wolfire  <https://orcid.org/0000-0003-0030-9510>
 M. W. Pound  <https://orcid.org/0000-0002-7269-342X>
 E. Tarantino  <https://orcid.org/0000-0003-1356-1096>
 R. Karim  <https://orcid.org/0000-0001-8844-5618>
 L. Bonne  <https://orcid.org/0000-0002-0915-4853>
 C. Buchbender  <https://orcid.org/0000-0002-2064-7691>
 R. Güsten  <https://orcid.org/0000-0002-1708-9289>
 Ü. Kavak  <https://orcid.org/0000-0002-7640-4998>
 N. Schneider  <https://orcid.org/0000-0003-3485-6678>
 R. Simon  <https://orcid.org/0000-0003-2555-4408>
 J. Stutzki  <https://orcid.org/0000-0001-7658-4397>
 A. G. G. M. Tielens  <https://orcid.org/0000-0003-0306-0028>

References

- Ascenso, J., Alves, J., Beletsky, Y., & Lago, M. T. V. T. 2007, *A&A*, **466**, 137
 Benaglia, P., Koribalski, B., Peri, C. S., et al. 2013, *A&A*, **559**, A31
 Benjamin, R. A., Churchwell, E., Babler, B. L., et al. 2003, *PASP*, **115**, 953
 Beuther, H., Schneider, N., Simon, R., et al. 2022, *A&A*, **659**, A77
 Bonne, L., Schneider, N., García, P., et al. 2022, *ApJ*, **935**, 171
 Castellanos, P., Berné, O., Sheffer, Y., Wolfire, M. G., & Tielens, A. G. G. M. 2014, *ApJ*, **794**, 83
 Churchwell, E., Whitney, B. A., Babler, B. L., et al. 2004, *ApJS*, **154**, 322
 Dagdigan, P. J. 2019, *JChPh*, **151**, 054306
 Draine, B. T. 2003, *ARA&A*, **41**, 241
 Foreman-Mackey, D. 2016, *JOSS*, **1**, 24
 Furukawa, N., Dawson, J. R., Ohama, A., et al. 2009, *ApJL*, **696**, L115
 Gerin, M., Ruaud, M., Goicoechea, J. R., et al. 2015, *A&A*, **573**, A30
 Goicoechea, J. R., Teyssier, D., Etxaluze, M., et al. 2015, *ApJ*, **812**, 75
 Goldsmith, P. F., Langer, W. D., Seo, Y., et al. 2021, *ApJ*, **916**, 6
 Güsten, R., Nyman, L., Schilke, Å., et al. 2006, *A&A*, **454**, L13
 Heays, A. N., Bosman, A. D., & van Dishoeck, E. F. 2017, *A&A*, **602**, A105
 Hollenbach, D., Kaufman, M. J., Neufeld, D., Wolfire, M., & Goicoechea, J. R. 2012, *ApJ*, **754**, 105
 Hollenbach, D. J., & Tielens, A. G. G. M. 1999, *RvMP*, **71**, 173
 Houck, J. R., Roellig, T. L., van Cleve, J., et al. 2004, *ApJS*, **154**, 18
 Joblin, C., Bron, E., Pinto, C., et al. 2018, *A&A*, **615**, A129
 Kabanovic, S., Schneider, N., Ossenkopf-Okada, V., et al. 2022, *A&A*, **659**, A36
 Kaufman, M. J., Wolfire, M. G., & Hollenbach, D. J. 2006, *ApJ*, **644**, 283
 Kavak, U., Goicoechea, J. R., Pabst, C. H. M., et al. 2022, *A&A*, **660**, A109
 Klein, B., Hochgürtel, S., Krämer, I., et al. 2012, *A&A*, **542**, L3
 Kovalenko, A., Dung Tran, T., Rednyk, S., et al. 2018, *ApJ*, **856**, 100
 Lique, F., Klos, J., Alexander, M. H., Le Picard, S. D., & Dagdigan, P. J. 2018, *MNRAS*, **474**, 2313
 Liseau, R., Justtanont, K., & Tielens, A. G. G. M. 2006, *A&A*, **446**, 561
 Luisi, M., Anderson, L. D., Schneider, N., et al. 2021, *SciA*, **7**, eabe9511
 Milam, S. N., Savage, C., Brewster, M. A., Ziurys, L. M., & Wyckoff, S. 2005, *ApJ*, **634**, 1126
 Mohr-Smith, M., Drew, J. E., Barentsen, G., et al. 2015, *MNRAS*, **450**, 3855
 Molinari, S., Swinyard, B., Bally, J., et al. 2010, *PASP*, **122**, 314
 Neufeld, D. A., & Wolfire, M. G. 2016, *ApJ*, **826**, 183
 Neufeld, D. A., & Wolfire, M. G. 2017, *ApJ*, **845**, 163
 Ohama, A., Dawson, J. R., Furukawa, N., et al. 2010, *ApJ*, **709**, 975
 Pabst, C., Higgins, R., Goicoechea, J. R., et al. 2019, *Natur*, **565**, 618
 Pabst, C. H. M., Goicoechea, J. R., Hacar, A., et al. 2022, *A&A*, **658**, A98
 Pabst, C. H. M., Goicoechea, J. R., Teyssier, D., et al. 2017, *A&A*, **606**, A29
 Poglitsch, A., Herrmann, F., Genzel, R., et al. 1996, *ApJL*, **462**, L43
 Poglitsch, A., Waelkens, C., Geis, N., et al. 2010, *A&A*, **518**, L2
 Pound, M. W., & Wolfire, M. G. 2008, in ASP Conf. Ser. 394, Astronomical Data Analysis Software and Systems XVII, ed. R. W. Argyle, P. S. Bunclark, & J. R. Lewis (San Francisco, CA: ASP), 654
 Pound, M. W., & Wolfire, M. G. 2011, PDRT: Photo Dissociation Region Toolbox, Astrophysics Source Code Library, ascl:1102.022
 Rauw, G., Crowther, P. A., De Becker, M., et al. 2005, *A&A*, **432**, 985
 Rauw, G., Sana, H., & Nazé, Y. 2011, *A&A*, **535**, A40
 Risacher, C., Güsten, R., Stutzki, J., et al. 2018, *JAI*, **7**, 1840014
 Rosenberg, M. J. F., van der Werf, P. P., Aalto, S., et al. 2015, *ApJ*, **801**, 72
 Salgado, F., Berné, O., Adams, J. D., et al. 2016, *ApJ*, **830**, 118
 Sander, A., Shenar, T., Hainich, R., et al. 2015, *A&A*, **577**, A13
 Schneider, N., Röllig, M., Simon, R., et al. 2018, *A&A*, **617**, A45
 Schneider, N., Simon, R., Guevara, C., et al. 2020, *PASP*, **132**, 104301
 Schuller, F., Menten, K. M., Contreras, Y., et al. 2009, *A&A*, **504**, 415
 Seo, Y. M., Goldsmith, P. F., Walker, C. K., et al. 2019, *ApJ*, **878**, 120
 Smith, J. D. T., Armus, L., Dale, D. A., et al. 2007a, *PASP*, **119**, 1133
 Smith, J. D. T., Draine, B. T., Dale, D. A., et al. 2007b, *ApJ*, **656**, 770
 Tielens, A. G. G. M. 2005, The Physics and Chemistry of the Interstellar Medium (Cambridge: Cambridge Univ. Press)
 Tiwari, M., Karim, R., Pound, M. W., et al. 2021, *ApJ*, **914**, 117
 Townsley, L. K., Broos, P. S., Garmire, G. P., & Povich, M. S. 2019, *ApJS*, **244**, 28
 Tran, T. D., Rednyk, S., Kovalenko, A., et al. 2018, *ApJ*, **854**, 25
 Tsujimoto, M., Feigelson, E. D., Townsley, L. K., et al. 2007, *ApJ*, **665**, 719
 Vargas Álvarez, C. A., Kobulnicky, H. A., Bradley, D. R., et al. 2013, *AJ*, **145**, 125
 Werner, M. W., Roellig, T. L., Low, F. J., et al. 2004, *ApJS*, **154**, 1
 Whiteoak, J. B. Z., & Uchida, K. I. 1997, *A&A*, **317**, 563
 Whitney, B. A., Indebetouw, R., Babler, B. L., et al. 2004, *ApJS*, **154**, 315
 Wolfire, M. G., McKee, C. F., Hollenbach, D., & Tielens, A. G. G. M. 2003, *ApJ*, **587**, 278
 Wolfire, M. G., Vallini, L., & Chevance, M. 2022, arXiv:2202.05867
 Wu, R., Bron, E., Onaka, T., et al. 2018, *A&A*, **618**, A53
 Young, E. T., Becklin, E. E., Marcum, P. M., et al. 2012, *ApJL*, **749**, L17
 Young Owl, R. C., Meixner, M. M., Fong, D., et al. 2002, *ApJ*, **578**, 885
 Zeidler, P., Sabbie, E., Nota, A., et al. 2015, *AJ*, **150**, 78